A novel approach to the study of extensional flow-induced crystallization

Juliana Amirdine, Thouaïba Htira, Nicolas Lefevre, René Fulchiron, Nathalie Mathieu, Matthieu Zinet, Christophe Sinturel, Teodor Burghelea, Nicolas Boyard

Version of Record: https://www.sciencedirect.com/science/article/pii/S0142941821000106
Manuscript_decaa2659a756799f1f9b822959872e7

A novel approach to the study of extensional flow-induced crystallization

Juliana Amirdine,[1] Thouaïba Htira,[2] Nicolas Lefevre[1], René Fulchiron,[2] Nathalie Mathieu,[3] Matthieu Zinet,[2] Christophe Sinturel,[3] Teodor Burghelea,[1] Nicolas Boyard[1]

[1] *Université de Nantes, CNRS, Laboratoire de Thermique et Energie de Nantes, UMR 6607, La Chantrerie, Rue Christian Pauc, F-44000 Nantes, France*

[2] *Univ Lyon, Université Claude Bernard Lyon 1, CNRS, IMP UMR 5223, F-69622, Villeurbanne, France*

[3] *Interfaces, Confinement, Matériaux et Nanostructures (ICMN) UMR 7374, CNRS-Université d'Orléans, CS 40059, F-45071 Orléans, France*

Abstract

A systematic experimental investigation of the coupling between the extensional flow and the crystallisation of a commercial grade polypropylene is presented. A modified Sentmanat extensional device allows one to generate a uniaxial extensional flow in the absence of gravity sagging and monitoring its effect on the kinetics of crystallisation via in-situ visualisation of the sample in polarised light. As compared to the shear induced crystallisation, a three fold increase of the kinetics of the extension induced crystallisation is found. The study is complemented by a post mortem analysis of the crystalline morphology by small angle X ray scattering ($SAXS$) and wide angle X ray scattering ($WAXS$).

Keywords: extensional flow, flow induced crystallisation, modified SER fixture

Contents

Email address: Nicolas.Boyard@univ-nantes.fr (Juliana Amirdine,[1] Thouaïba Htira,[2] Nicolas Lefevre[1], René Fulchiron,[2] Nathalie Mathieu,[3] Matthieu Zinet,[2] Christophe Sinturel,[3] Teodor Burghelea,[1] Nicolas Boyard[1])

List of Figures

1. Introduction

Polymer forming processes such as injection molding, extrusion or film blowing are widely used in the plastic industry. During the forming process, the plastic undergoes a phase change which takes place under different conditions of pressure, flow and cooling rate. The processing conditions (pressure Angelloz et al. (2000), cooling rate S. A. E. Boyer and Haudin (2010), S. A. E. Boyer et al. (2012) and flow Lagasse and Maxwell (1976)Wang et al. (2016)) impact the crystallization phenomenon in terms of its kinetics and crystalline microstructure. The phenomenon of flow-induced crystallization (FIC) has been widely studied in the literature Eder et al. (1990) McHugh (1995), Koscher and Fulchiron (2002). Beyond a critical shear rate the shear-induced crystallization (SIC) shows an acceleration of the kinetics manifested through an increase in the number of nuclei Lagasse and Maxwell (1976) Koscher and Fulchiron (2002), Hadinata et al. (2005). The flow also impacts the microstructure by orienting it along its direction which sometimes leads to the formation of a highly oriented microstructure called shish-kebab Janeschitz-Kriegl and Ratajski (2005) Wang et al. (2016), Roozemond et al. (2016).

In the case of polypropylene which is a polymorphic polymer the flow may also lead to the formation of the β-phase in addition to the classical α-phase, Koscher (2002). In addition, some authors show that the processing conditions

accelerate the associated crystallization kinetics Sentmanat et al. (2010),Derakhshandeh and Hatzikiriakos (2012),White et al. (2012). These kinetics are of primary importance for the process simulation. Thus, appropriate models need to be developed and used in order to describe various processing settings. The modification of the microstructure and the kinetics of crystallization under flow need to be accounted for in order to simulate polymer processing operations. While crystallization in quiescent conditions is easily modelled by the well known formalism of Avrami Avrami (1939), Avrami (1940), Avrami (1941), the flow induced crystallization remains elusive and new models need to be developed. Schneider Schneider et al. (1988) suggests taking into account the flow from a differential approach or the work of Peters Roozemond et al. (2016) or that of Haudin-Chenot Boyer et al. (2011) may explain the presence of different crystalline phases.

The extension is the dominant flow during many polymer processing operations including melt blowing, extrusion and fibre spinning, Muke et al. (2001), Sentmanat (2004), Stary et al. (2015). Unlike shear flows, extensional flows are clearly more complex and their laboratory implementation is rather non trivial. Quite often, one can not generate a purely extensional flow but a mixture of shear and extension. Several devices used to study the response of polymeric materials to extensional flow were then developed: the Rheometrics Melt Rheometer (RME) by Meissner Meissner and Hostettler (1994), the Münstedt Tensile Rheometer (MTR) by Münstedt Münstedt and Laun (1979), or the Sentmanat Extensional Rheometer (SER) Sentmanat (2004) and the Filament Stretching Rheometer (FISER) Bach et al. (2002), Szabo and McKinley (2003), Iannirubertо et al. (2020). Among these devices, only the SER tool is commercially available and can be easily mounted on any rotational rheometer.

As opposed to the case of shear flow, there exist very few studies of the coupling between crystallisation and the extensional flow. This might be explained by the fact that in order to study the crystallisation a number of modifications of the extensional devices are needed. As an example, Bischoff White and coworkers have studied the extension induced crystallisation using a modified $FISER$ device, White et al. (2012). They observe an acceleration of kinetics of crystallisation for extensional rates exceeding a critical value. Other studies I propose the construction of new extensional setups inspired by the SER, Liu et al. (2011), Liu et al. (2014), Tian et al. (2011), Tian et al. (2013). A heating system using ionic liquid combined with optically transparent walls allows an in-situ analysis of the crystaline microstructure during extension. However, these studies do not address the coupling before the microstructure and the kinetics of crystallisation.

There exist few studies dealing with this coupling Hadinata et al. (2007), Chellamuthu et al. (2011), Derakhshandeh and Hatzikiriakos (2012), White et al. (2012), Liu et al. (2011), Liu et al. (2014), Tian et al. (2011), Tian et al.

(2013). Their studies show a mainly *post-mortem* or *in-situ* characterization of the crystalline microstructure using classical DSC and X-ray scattering techniques ($SAXS$ and $WAXS$). The extension generates a strong orientation of the crystalline lamellae in the direction of flow and an increase in the number of nuclei. However, a quantitative assessment of the kinetics of crystallization and its relation to the properties of the extensional flow is largely absent in the literature. Such an assessment is of paramount importance for developing a theoretical framework for the EIC and its further numerical implementation. The present study proposes a systematic experimental characterization of the crystallization induced by extensional flow in both an *in-situ* and *post-mortem* fashion. The use of polarized light *in-situ* characterization tool allows one to assess the characteristic time scales associated to the crystallization and to compare them with the times of semi-crystallization obtained in either quiescent conditions or during a shear flow. The characterization of the microstructure and of the induced crystal phases is also performed.

The paper is organised as follows. The choice of the working polymeric material and the description of the experimental methods are detailed in Sec. 2. The experimental results are presented in Sec. 3. The crystallisation in quiescent conditions is discussed in Sec. 3.1. The shear induced crystallisation is investigated in Sec. 3.2. The extension induced crystallisation is studied in Sec. 3.3. The assessment of the extension induced crystallisation via classical measurements of the transient elongational viscosity is presented in Sec. 3.3.1. An *in-situ* chracterisation of the crystallisation process by means of polarised light imaging of the sample undergoing an extensional deformation is presented in Sec. 3.3.2. A systematic investigation of the impact of the extensional conditions on the crystalline micro-structure by means of wide angle X-ray scattering (WAXS) and small angle X-ray scattering performed post mortem is presented in Sec. 3.3.3. The paper closes with a summary of the main findings and of the central conclusions of the study, Sec. 4.

2. Experimental methods

2.1. Choice of the polymeric material

The study of the extension induced crystallization was performed using a commercial grade isotactic polypropylene (iPP) from Lyondell-Basell ($MOPLEN\ HP556E$). The choice of this linear iPP was mainly motivated by its high molecular weight of $M_w = 527\ kg/mol$ which translates into a good sensitivity to extensional flow. In addition to this, this material is known to exhibit a relatively modest strain hardening behaviour under extensional flow which allows one to relate an apparent increase of the transient extensional viscosity to the flow induced crystallization. The polydispersity index is 5.3 Burghelea et al. (2012) and the

quiescent melting temperature is $T_m = 164^oC$.

2.2. Rheological characterisation in shear

The linear viscoelastic (LVE) properties of the iPP were determined using a strain-controlled rheometer Ares $G2$ (TA Instruments) equipped with a $25\ mm$ parallel plate geometry. Dynamic frequency sweeps were performed (100 to $0.01\ rad/s$, γ=5%) under nitrogen atmosphere at several temperatures ranging from 190^oC to 230^oC. Measurements of the storage modulus performed various temperatures are illustrated in Fig. 1.

The master curve was determined at 200^oC from an Arrhenius plot of the vertical shift factor a_T versus the inverse temperature $1/T$. In order to extract the activation energy from these measurements, a reference temperature $T = 200^oC$ has been chosen and the vertical shift factors a_T required to overlap the rest of the data sets onto the reference one have been obtained.The temperature dependence of the shift factors is illustrated in Fig. 2. The activation energy was found by fitting the dependence of the vertical shift factors on temperature by an Arrhenius law (the full line in Fig. 2) $E_a = 45.59\ kJ/mol$ (Fig. 2) which is in a fair agreement with results previously reported in the literature Koscher and Fulchiron (2002).

Last, the master curve was fitted by a N-mode ($N = 5$) Maxwell model (Eq. 2).

$$G'(\omega) = \sum_{i=1}^{N} G_i \frac{(\omega\lambda_i)^2}{1+(\omega\lambda_i)^2} \quad (1)$$

$$G''(\omega) = \sum_{i=1}^{N} G_i \frac{\omega\lambda_i}{1+(\omega\lambda_i)^2} \quad (2)$$

The parameters relaxation moduli G_i and and the relaxation times λ_i are listed in Table 1. The average relaxation time given by $\lambda_w = \frac{\sum G_i\lambda_i^2}{\sum G_i\lambda_i}$ was $\lambda_w = 19.3\ s$ at 200^oC.

λ_i [s]	$\mathbf{G_i[Pa]}$
$(2.8 \pm 2 \cdot 10^{-2}) \cdot 10^{-2}$	$(7.1 \pm 0.45) \cdot 10^4\ Pa$
$(2.5 \pm 5 \cdot 10^{-2}) \cdot 10^{-1}$	$(2.7 \pm 0.33) \cdot 10^4\ Pa$
(1.9 ± 0.24)	$(5.9 \pm 0.4) \cdot 10^3\ Pa$
$(1.4 \pm 0.2) \cdot 10^1$	$(6.9 \pm 1.2) \cdot 10^2\ Pa$
$(1.1 \pm 0.5) \cdot 10^2$	$(3.8 + 0.8) \cdot 10^1\ Pa$

Table 1: Relaxation spectrum for iPP at $200\ ^oC$.

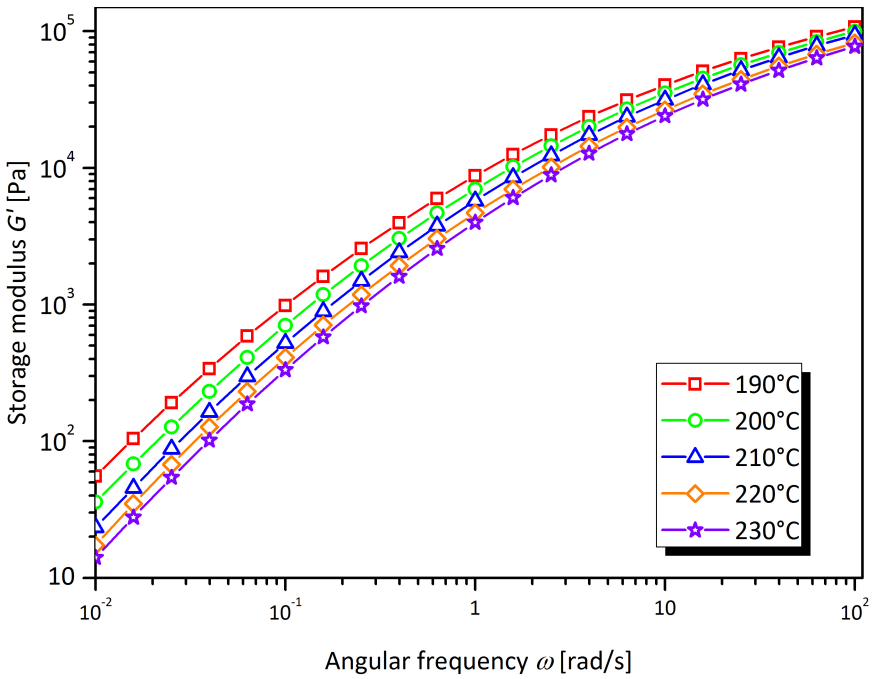

Figure 1: Dependence of the storage modulus G' on the oscillation frequency measured for several temperatures T indicated in the insert.

2.3. Quiescent crystallization (QC)

The kinetics of crystallization in quiescent conditions were investigated on a sample of approximately $7.5\ mg$ using Differential Scanning Calorimetry (DSC) (model $Q200$ from TA Instruments). The experimental protocol is presented Fig. 3. On this device, the achievable cooling speed is approximately $70\ K/min$. Thus, thanks to DSC, the crystallization kinetics of PP can be obtained in a range of temperatures between 130 and 142^oC because crystallization should not appear during cooling.

The relative crystallinity is determined by integrating the heat flux according to Eq. 3 where ϕ is the heat flux released at a given time and ΔH_{tot} the totale enthalpy of crystallization. The half-crystallization time $t_{1/2}$ was obtained for a relative crystallinity $\alpha = 0.5$. The initial time $t = 0$ was defined as the moment where the isothermal condition was reached.

$$\alpha(t) = \frac{\int_0^t \phi(\tau) d\tau}{\Delta H_{tot}} \tag{3}$$

To assess the kinetics of crystallization at lower temperatures, Fast Scanning Calorimetry (FSC) Adamovsky et al. (2003)Zhuravlev and Schick (2010a)Zhuravlev and Schick (2010b) is performed in a nitrogen gas atmosphere using a Flash DSC1

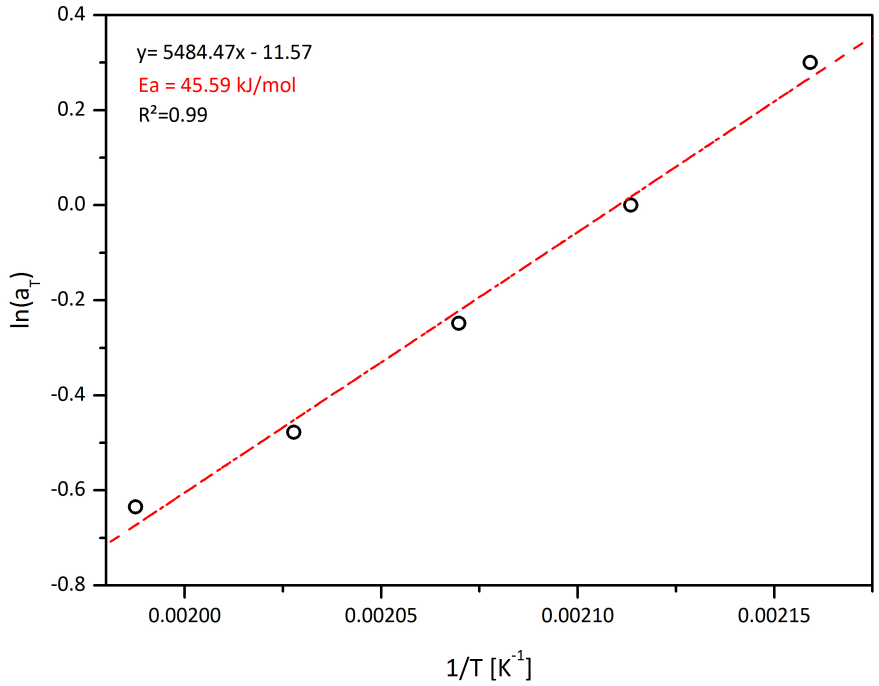

Figure 2: Dependence of the shift factor on temperature. The full line is a linear fit function $ln\,(a_T) = a(\pm\delta a)\frac{1}{T} + b(\pm\delta b)$.

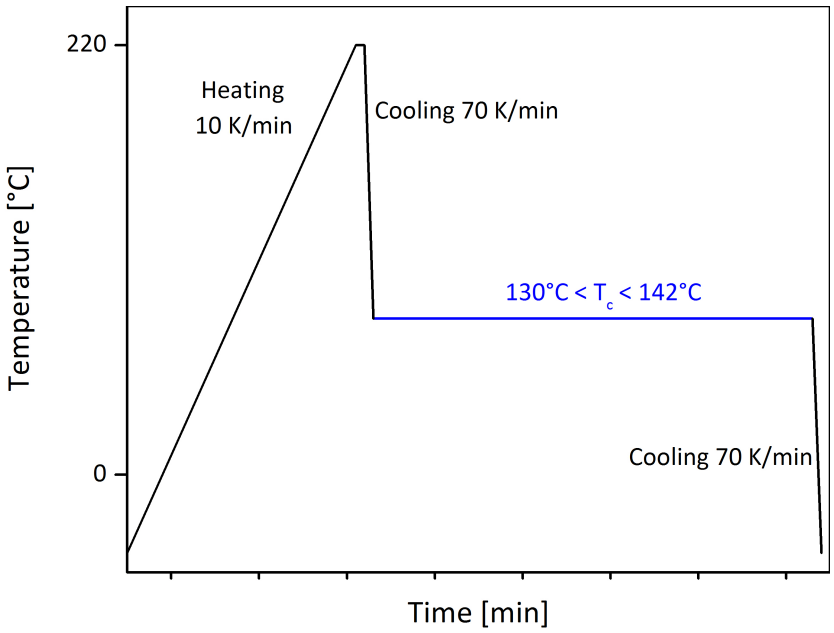

Figure 3: Diagram of the temperature cycle for DSC apparatus

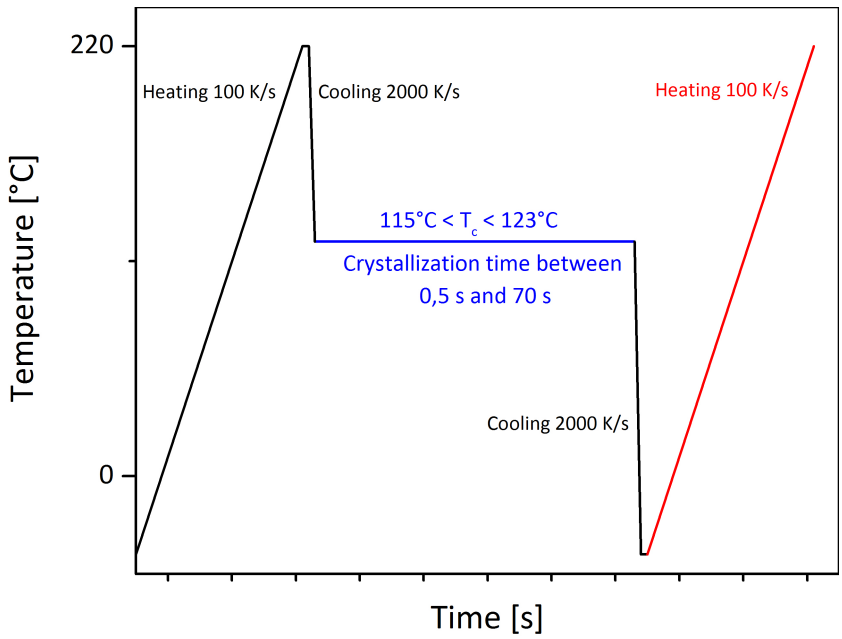

Figure 4: Experimental protocol for the discrete method in FSC

from Mettler Toledo. The mass of the sample is roughly $1\ \mu g$. FSC achieves much faster cooling rates than DSC and enables to impose a PP quenching rate (cooling) of $2000\ K/s$. Thus, the kinetics of crystallization of PP can be obtained according to the same protocol as in DSC but ranging from 5 and 110^oC. When the heat flux is too low, the discrete method described by Tardif et al. (2014) is used. It consists on repeating the isothermal crystallization while changing crystallization time. The melting enthalpy determined during the heating step is equivalent to the measure of the crystallization enthalpy during the previous isothermal step (Fig. 4).

Thanks to the DSC and FSC measurements, the kinetics of crystallization of PP can be studied by determining the half-crystallization time over a large temperature range.

2.4. Shear Induced crystallization (SIC)

To study shear flow, the classical Janeschitz-Kriegl thermal protocol was used (Fig. 5).

The shear induced crystallization (SIC) was studied using the same rheometer used for the rheological characterisation in shear. The polymer pellets were first maintained at 220^oC for $5\ min$ in a $8\ mm$ diameter cone-plate $0.1\ rad$ geometry with a gap equal to $0.051\ mm$. Then the sample was cooled down as fast as possible to the expected temperature (isothermal condition). For each

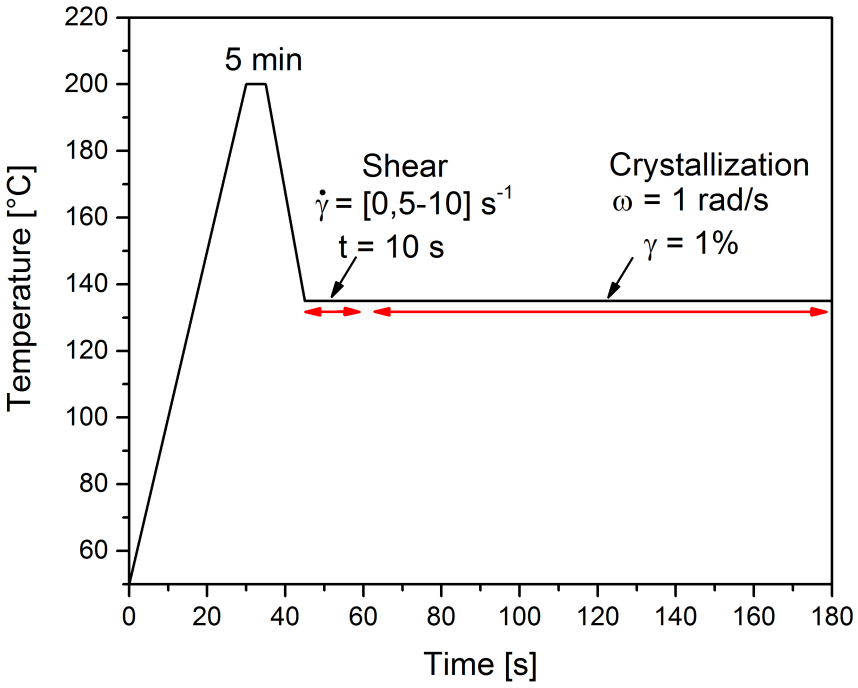

Figure 5: Diagram of the temperature cycle

temperature, a shear rate between $0.5\ s^{-1}$ to $10\ s^{-1}$ was applied for $t_s = 10\ s$, a time which is high enough to have a significant effect on the orientation of the macromolecular chains (Koscher (2002), Karpp-Pfordt (2006)). The crystallization was tracked through the response of the sample to an oscillatory strain with a frequency $\omega = 1\ rad/s$ (γ=1%). The experiments were carried on under nitrogen gas to avoid thermal oxydation of the iPP. The half-crystallization time was estimated according to the semi-empirical rule proposed by Koscher (2002) to:

$$logG'_{t_{1/2}} = \frac{log\,(G'_{max}) + log\,(G'_{min})}{2} \tag{4}$$

The gap is adjusted in real time to avoid the experimental artefacts induced by the shrinkage of the sample during the crystallization process. The onset time of crystallization t_{onset} was defined by the time corresponding to an increase of the storage modulus.

2.5. Extensional-flow Induced crystallization (EIC)

A Sentmanat Extensional Rheometer (SER) Sentmanat (2004) device was installed on a Haake Mars III rheometer (from ThermoFischer Scientific) to study the extensional-flow Induced crystallization (EIC). It consists on two rotating

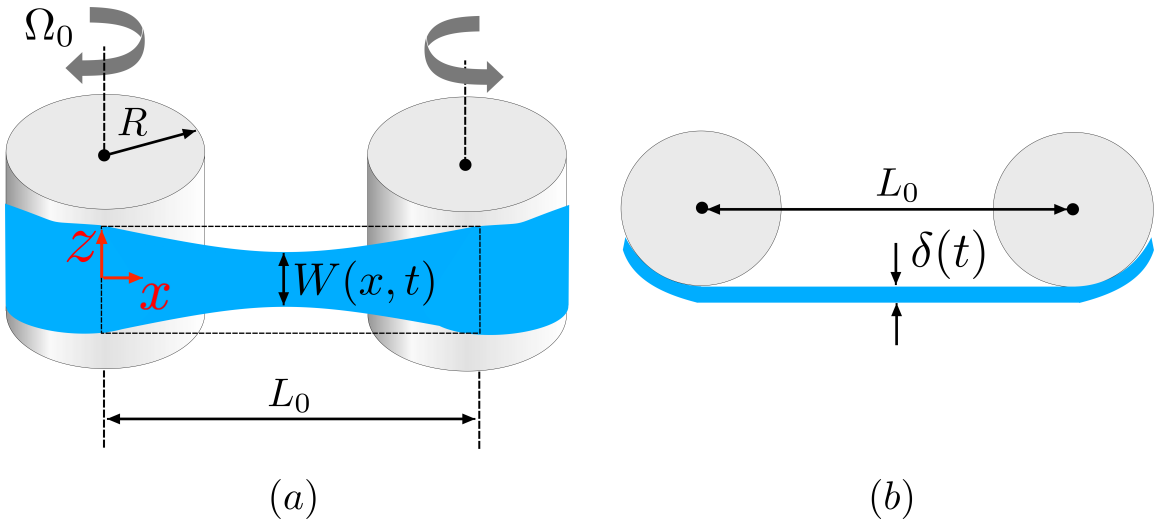

Figure 6: Schematic view of the Sentmanat extensional rheometer (SER) during operation

cylindrical drums of radius R separated by a distance L_0. They were inter-coupled by a system of gears such as the rotation of the cylinder connected to the shaft triggers the rotation of the second cylinder at a same angular speed but in an opposite direction (Fig. 6). For all the experiments reported herein a rectangular sample with dimensions $18\ mm \times 10\ mm \times 0.50\ mm$ was used. The iPP sample was moulded by compression at 200^oC for 5 minutes to erase the thermal history and then cooled down at 140^oC. The sample was then fixed on the outer surface of the rotating cylinders with two thin stainless steel clamps. For a constant angular speed of the shaft of the rotational rheometer, Ω, the Hencky strain rate experienced by the sample is expressed according to Eq.5):

$$\dot{\epsilon}_H = \frac{2\Omega R}{L_0} \tag{5}$$

The transient uniaxial extensional viscosity is defined as $\eta_e^+ = \frac{\sigma_e^+(t)}{\dot{\epsilon}_H}$ where the transient extensional stress σ_e^+ is defined as:

$$\sigma_e^+(t) = \frac{M}{2RA(t)exp(-\dot{\epsilon}_H t)} \tag{6}$$

In the equation above M is the torque measured by the rotational rheometer, $A(t)$ is the cross-sectional area of the sample as a function of temperature:

$$A(t) = A_0 exp\left(\frac{\rho_s}{\rho_m(T)}\right)^{2/3} \tag{7}$$

where ρ_s is the sample density at solid state ($845\ kg/m^3$ at 20^oC), $\rho_m(T)$ is the melt density at temperature T (determined from PvT diagram; as an example, at 200^oC $\rho_m(T)$ is equal to $748\ kg/m^3$), and A_0 is the initial cross-sectional area of the sample. The total deformation of the sample is limited to a maximum Hencky strain of $\epsilon_H^{max} = 4$ because the fixing clamps come into contact after three-quarter turn. The measurements were carried out at Hencky strain rates from $0.05\ s^{-1}$ to $10\ s^{-1}$.

The Sentmanat device was initially designed for the characterisation of elastomers rather than of polymer melts Sentmanat (2004). When used with molten polymeric samples there are two important drawbacks to be aware of. First, the samples are heated using a convection oven mounted on the rotational rheometer. Thus, the homogeneity of the temperature distribution of the sample may be problematic and, for the commercially available ovens, practically impossible to assess quantitatively. Second, as the sample is held in air, gravity sagging effects bias the extensional tests particularly in a range of low rates of extension Sentmanat (2004)Liu et al. (2011). As the walls of the oven are not optically transparent, the geometric homogeneity of the sample can not be visually assessed.

To circumvent these practical limitations, a custom-made oil bath to submerge the Sentmanat device was fitted to the rotational rheometer (Fig. 7). Through the bath with a volume $65\ mL$ thermally stabilised, silicon oil is continuously circulated which plays three important roles. First, this addition allows one to ensure a homogeneous distribution of temperature within the sample. Second, as the density of the silicon oil is close to that of the molten polymeric sample, the gravity sagging effects are practically eliminated. This experimental trick was already used by other authors (Liu et al. (2011), Münstedt et Laun (1979)) and the question of possible interaction between the liquid and the specimen was never addressed. The use of the liquid with a density similar to the sample one is the only way to avoid the gravity sagging effect.

Third and foremost, the front/back glass windows of the oil bath allow an *in-situ* analysis of the extension induced crystallization by means of polarised light imaging of the sample during extension. The temperature cycle performed in SIC is retained (Fig. 5), however the cooling rate remains slower ($10\ K/min$) in the case of EIC measurements due to the thermoregulation capability of the oil bath.

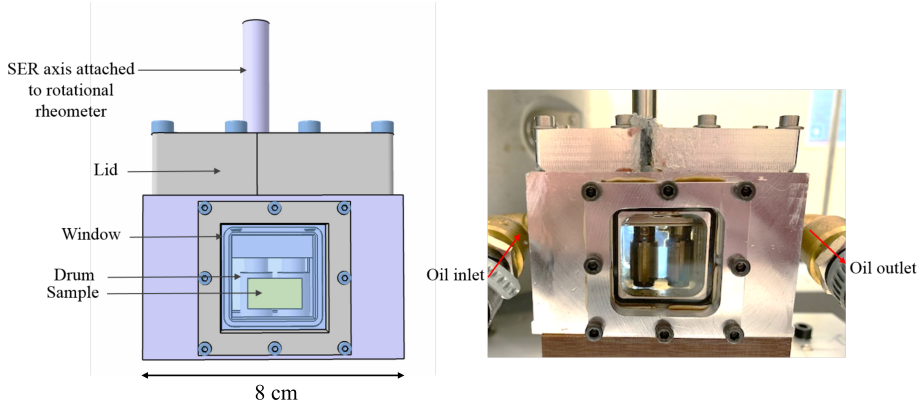

Figure 7: Schematic and real view of the Sentmanat extensional rheometer (SER) during operation

2.6. In-situ and post-mortem quantitative assessment of the extension induced crystallization

2.6.1. In-situ visualization with polarised light

An *in-situ* quantitative assessment of the extension induced crystallization is made by direct imaging of the sample in polarised light during the extensional process. The optical arrangement is inspired by Lamberti et al. (2004) and Oukaci-Boukellal (2010) and is schematically illustrated in Fig. 8 and may be described as follows. The sample is illuminated from behind through the back glass window of the oil bath by a white light source. Prior to traversing the sample, the white light is passed through a polarizer (90^o, $400 - 700\ nm$) and a quarter-wave plate. The light is collected through the front glass window of the oil bath by an analyzer (0^o, $400 - 700\ nm$) oriented at $\pi/2$ with respect to the polarisation axis of the polarizer and projected onto the sensor of a digital charged coupled device equipped with an appropriate focusing lens.

The kinetics of crystallization is quantitatively assessed by monitoring the intensity of the light received by the video camera (Chameleon, Flir) during the extensional flow experiment. The image acquisition process is synchronised with the data acquisition one performed by the rotational rheometer. The recording continues after the extensional flow. The light intensity is determined by a home-made matlab code (image processing toolbox) allowing the average of the gray levels determined in a fixed area of the image between the cylinders of the SER.

2.6.2. X-ray measurements

SAXS experiments were performed on a high resolution X-ray spectrometer Xeuss 2.0 from Xenocs company equipped with a 30W microfocus sealed tube (Cu target ($\lambda = 1.5418\mathring{A}$). The X-ray spot size on sample is about 1mm and

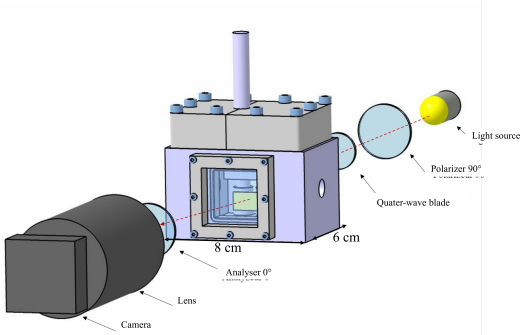

Figure 8: Schematic representation of the polarised light imaging system.

the incident flux of $6 \cdot 10^6$ photons per second. The SAXS patterns were record with a 2D high intensity low noise detector (Pilatus 300K hybrid pixel) placed at a distance of $2373\ mm$ from the sample, perpendicular to the X-ray beam (pixel size= $172\ \mu m$). The size of X-ray beam on sample is about $1\ mm$. The $2D\ SAXS$ patterns were recorded post-mortem after removing the extended sample from the SER device in a solid state. $1D\ SAXS$ profiles were extracted using FIT2D software within a q-range $0.08 - 1.7\ nm^{-1}$. and 1D profiles were corrected from background, incident flux, sample thickness ($0.3\ mm$), acquisition time (5 hours) and solid angle of detection Ω. The long period of the crystalline lamellae is called L_p and was estimated by $L_p = \frac{2\pi}{q_{max}}$ Angelloz et al. (2000).

Wide Angle-X-ray diffraction ($WAXS$) was performed at center of Diffractométrie Henri Longchambon (UCBL, Université Lyon 1) using a Oxford system with a copper source (wavelength of 1.54 Å). In order to determine the crystalline orientation, measurements were performed in transmission. The tube supplies $40\ eV$ and $30\ mA$. The exposure time was $390\ s$. The data were analyzed using the software Datasqueeze ($1D$ integration and plots as a function of azimutal angle).

3. Experimental results, discussion

3.1. Crystallization in quiescent conditions

The crystallization of the PP has been widely studied in quiescent conditions Koscher and Fulchiron (2002),De Santis et al. (2006),Mileva et al. (2012),Schawe (2015),Schawe et al. (2017) using DSC and FSC. We describe in the following similar measurements performed with PP samples crystallised in quiescent conditions. Following the protocols detailed in the previous section, the half-crystallization time versus temperature is plotted in Fig. 9.

According to Schawe (2015) and Schawe et al. (2017), iPP exhibits a bimodal kinetics with a phase transition at 65^oC. The α-phase, the most stable

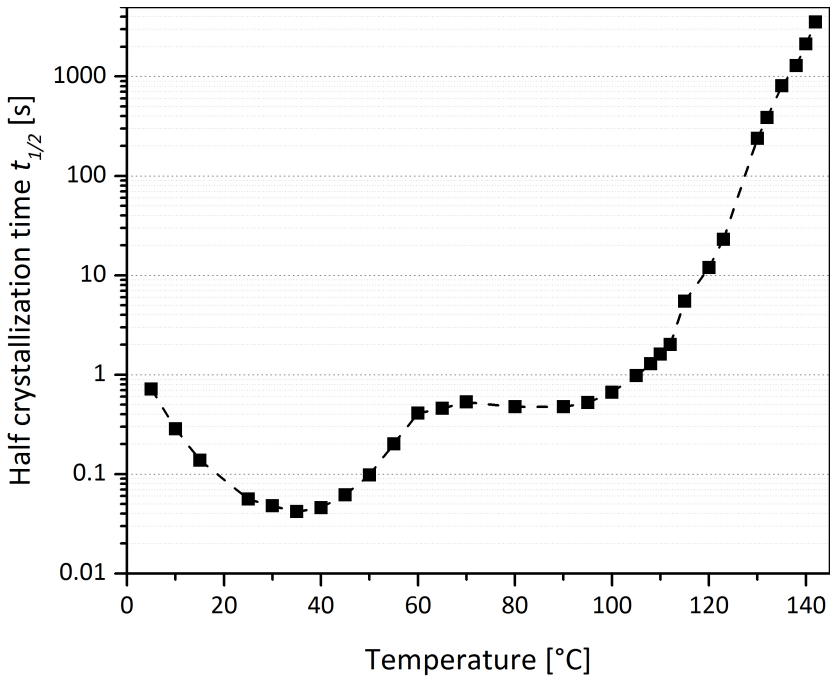

Figure 9: Half-crystallization time in quiescent condition obtain by DSC and Flash DSC

phase, is formed for low or medium supercooling at a crystallization temperature higher than 70^oC and for which the kinetics becomes faster. Below this limit, a mesophase is formed from a homogeneous nucleation mechanism and the half-crystallization time is increasing due to a low chain mobility. Unlike the α-phase, the mesophase is much less ordered or is considered even disordered by same authors Schawe (2015).

3.2. Shear-induced crystallization

The experimental results of the study of shear-induced crystallization are summarised in Fig. 10. The horizontal axis is divided in two distinct parts. The first one corresponds to an imposed shear for $10\ s$. The stress level (blue curves) increases with the shear rates. During the second stage of the tests after $10\ s$ (red curves), apart from the curve labelled as *emph"without shear"*, one observes first a drop in the storage modulus. This can be explained in terms of a relaxation of the polymer chains. Then, the curve of the storage modulus exhibits a shape which is qualitatively similar to the curve describing the evolution of the relative crystallinity, since it follows a sigmoidal evolution. The onset time of crystallization and the half-crystallization time can be determined from this part of the curve. Non-shear experiment was performed showing a good agreement with the half-crystallization times obtained in DSC in quiescent condition.

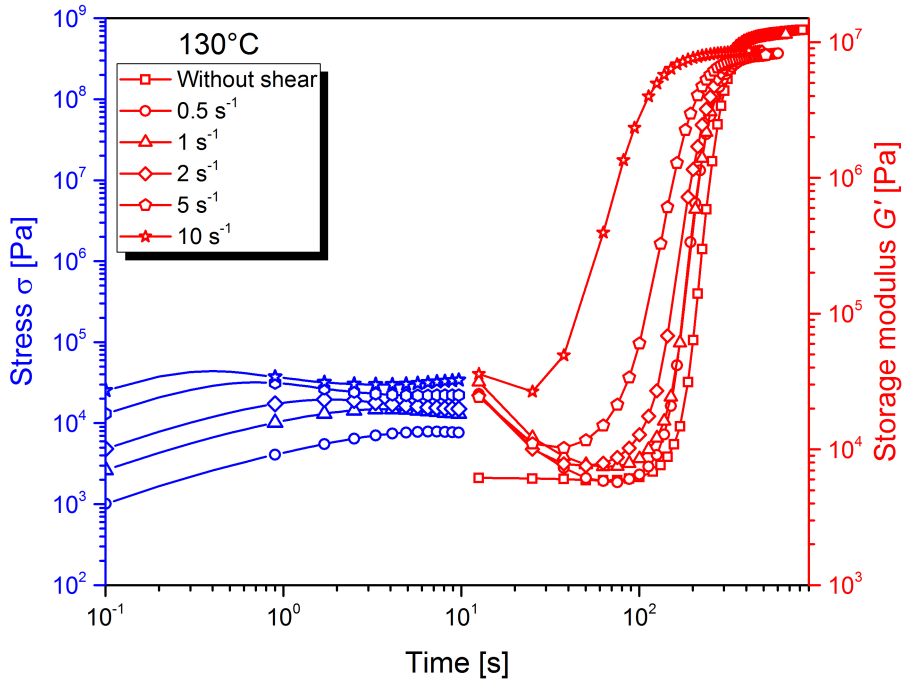

Figure 10: Isothermal crystallization monitored by the evolution of the elastic modulus after a pre-shearing step of $10\ s$ performed for several imposed rates of shear and at $T_c = 130^oC$.

The dependence of the half-crystallization time on the rate of shear plotted in Fig. 11 exhibits a plateau region for the quiescent half-crystallization time (positioned at $\dot{\gamma} = 10^{-3}\ s^{-1}$) up to about $1\ s^{-1}$ followed by a decrease of the half-crystallization time independently on the temperature. One notes that a critical shear rate exists beyond which the kinetics of cristallization is accelerated, $\dot{\gamma}_c \approx 4\ s^{-1}$. This behaviour is well known in the literature basing on the onset time of the storage modulus increase for a polyethylene by Lagasse and Maxwell (1976) or a poly-1-butene by Hadinata et al. (2005). Koscher and Fulchiron (2002) and Naudy et al. (2007) made the same observation for the half-crystallization time for a PP and a polyamide respectively.

3.3. Crystallization under extensional flow

3.3.1. Measurements of the transient extensional viscosity

Fig. 12 presents the extensional viscosity at 135^oC for differents Hencky strain rates and a Hencky strain of $\epsilon_H = 4$. For each rate of extension, the extensional viscosity changes in a similar way, until a sudden increase in the extensional viscosity called strain-hardening. The Trouton's law represents the linear viscoelastic response for uniaxial extension and is given by $\eta_e^+ = 3\eta_0$ where η_0 is the viscosity obtained from rotational rheometry in the newtonian domain.

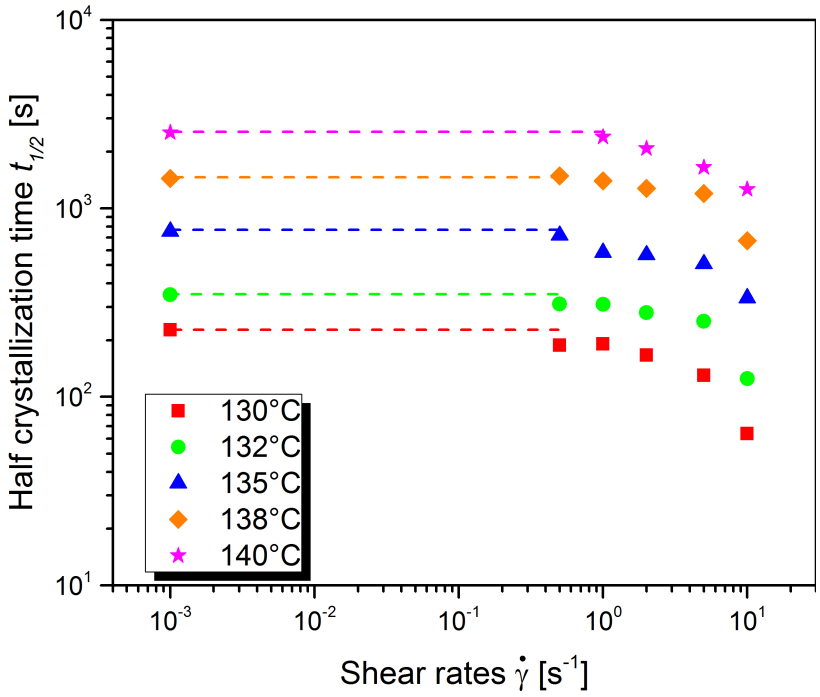

Figure 11: Half time crystallization for different pre-shear rates ($t_s = 10\ s$) and temperatures. The dotted lines illustrate a plateau over which, the crystallization is not affected by the pre-shear rate.

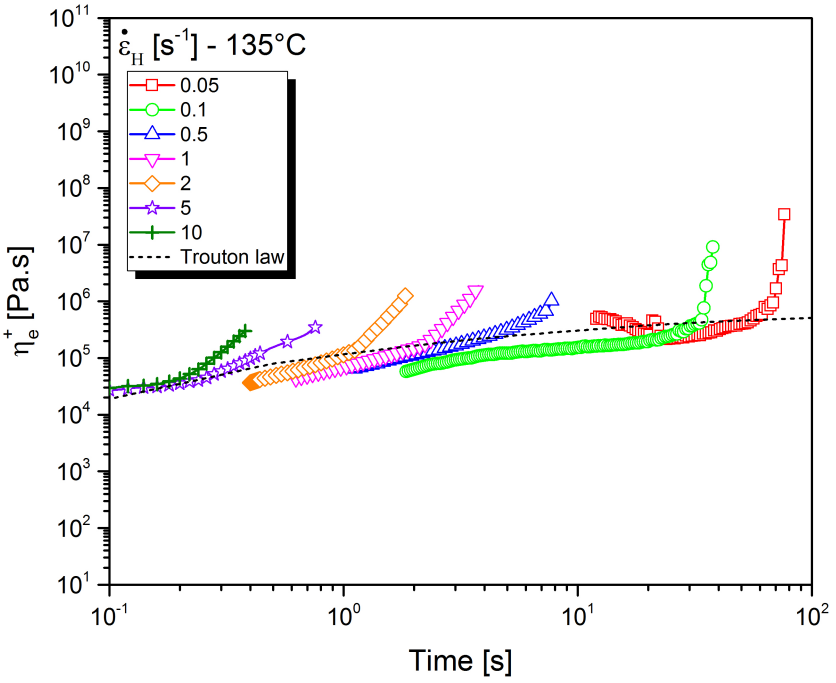

Figure 12: Extensional viscosity at $135\ ^oC$ for different Hencky strain rates, the black dashed lign represents the linear viscoelastic response obtained by Trouton's law

For temperatures below the melting temperature, it is not possible to carry out a frequency sweep over long times because crystallization would appear. Therefore, the Trouton's law is calculated according to the Maxwell model ($n_i = G_i\lambda_i$), whose parameters are given in Table 1:

$$\eta_e^+ = 3\sum_{i=1}^{N} n_i \left[1 - exp^{\frac{-t}{\lambda_i}}\right] \tag{8}$$

A strain-hardening behaviour is observed for all the rates of extension $\dot{\epsilon}_H$ investigated. The intensity of strain-hardening increases when the rates of extension decreases. This behaviour depends on the molar mass of the molten, polymer as highlighted by Stadler et al. (2009).

Hadinata et al. (2007) suggests to plot the onset times of strain-hardening increase as a function of the extension rate to quantify the presence of crystallization. The onset of strain-hardening (or crystallization) is determined when the extensional viscosity deviates from the Trouton's law. Fig. 13 compares the onset time at 200^oC and 135^oC versus the Hencky strain rates and the Weissenberg number ($Wi = \dot{\epsilon}_H \times \lambda_w$). The onset time t_{onset} in quiescent conditions indicated in the figure is the time of the beginning of crystallisation obtained by

DSC during an isothermal step at 135^oC. At 200^oC, iPP is completely molten while at 135^oC crystallization may occur. t_{onset} decreases linearly with the increase of the extension rate. A slight effect of the temperature on the onset times may be observed only for the smallest Hencky strain rates (lower than $1\ s^{-1}$) we have explored which correspond to the longest experimental time. Based on this macroscopic observation, one could assume that crystallization occurs for numbers Wi smaller than 122 at 135^oC. For low Hencky strain rates, the macromolecular chains are stretched longer and remain longer in the oil bath, inducing a possible effect of crystallization ont the extensional viscosity for these extension rates in addition to the strain-hardening. However, this analysis can be discussed because crystallization could also start well before the apparition of strain-hardening. On the contrary, for higher rates of extension, the measurement time is decreasing, so it is possible that it is not long enough to recover an effect of the crystallisation on the extensional viscosity. With the SER tool the tensile force can only be recorded during the flow, not after.

Finally, it is clear that it is not possible to conclude definitely about crystallization, based on the extensional viscosity curves only. At this point, we believe that the crystallisation occurs after the elongation.

3.3.2. In situ characterization by using polarized light

The oil bath and the polarised light imaging system allow one to follow the crystallization *in-situ* by monitoring the intensity of the flow induced birefringence FIB. The measurements are carried out at 133^oC up to a final Hencky strain of 2.5 so as not to obstruct the optical path between the cylindrical drums. The maximal rate of extension achievable with our rheometer is $\dot{\epsilon}_H^{max} = 2\ s^{-1}$. The measured light intensity I of each subsequent image is measured in a fix rectangle (red dotted lines in Fig. 14) and normalised by the light intensity I_0 measured without the sample. Images of the sample acquired during and after extension and the light intensity are illustrated in Fig. 14 and Fig. 15, respectively.

First, an increase of the light intensity is observed during the application of the extensional flow. This can be explained first by the decrease of the thickness of the sample ($0.51\ mm$ to $0.30\ mm$) during the test. However, this behaviour was also observed during the SIC experiments. The extensional flow aligns the polymer chains, thus creating an optically anisotropic behaviour named flow induced birefringence (FIB). Moreover, the light intensity increases more and more with the Hencky strain rate. Indeed, the extension mechanism is exponential in time unlike shear. The extensional flow therefore aligns the chains more, which promotes nucleation, or even strongly oriented microstructures.

At the end of the extensional process, the light intensity decreases due to the relaxation of the macromolecular chains. At this point, it is interesting to correlate this result with the extensional viscosity behaviour; if the crystalliza-

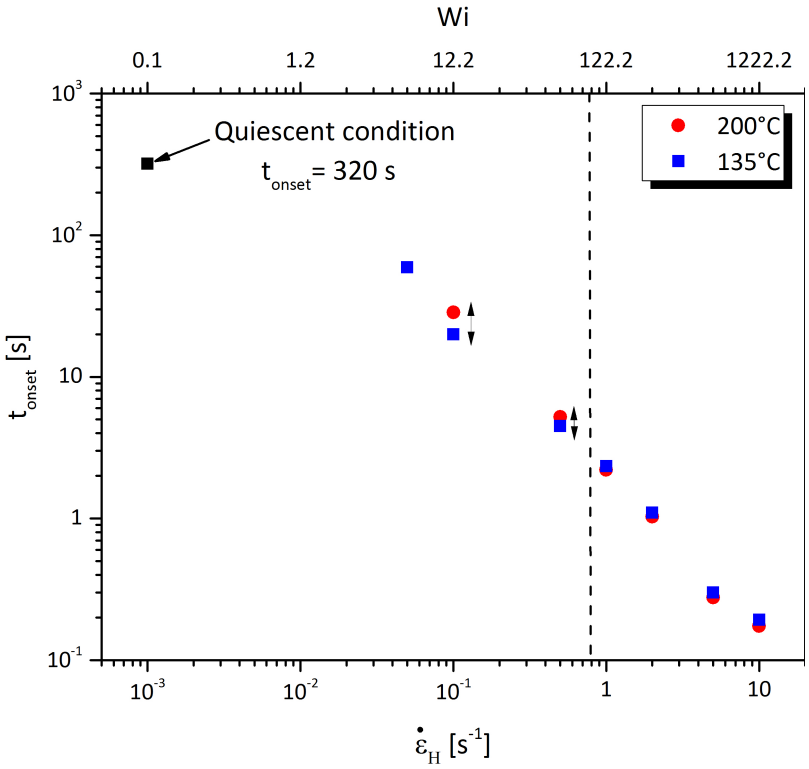

Figure 13: Onset time measured at $200\ ^oC$ (circles) and $135\ ^oC$ (squares) for different Hencky strains. The corresponding Weissenberg numbers are displayed on the top axis.

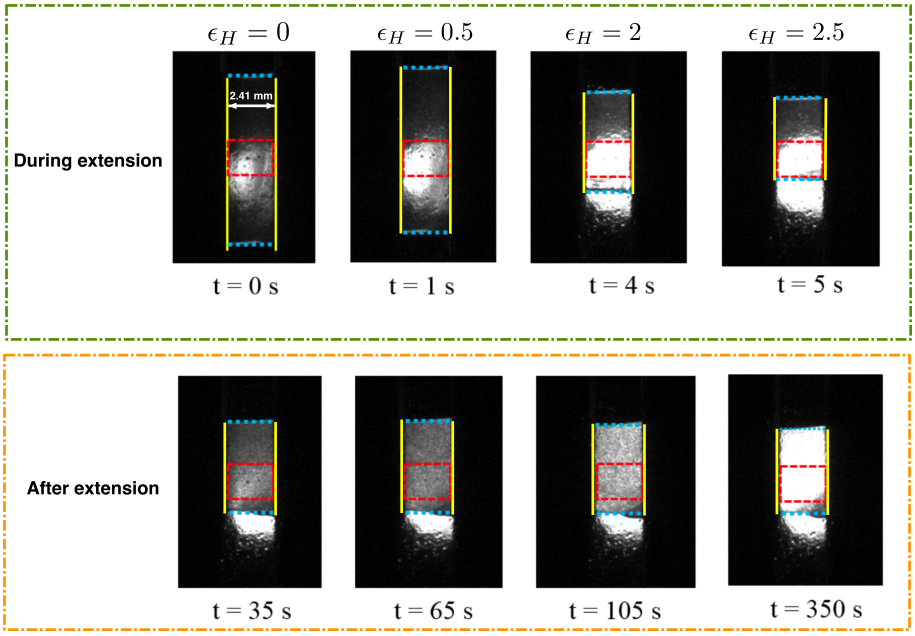

Figure 14: Light intensity during and after the extensional flow at $133\ ^oC$, $\dot{\epsilon}_H = 0.5\ s^{-1}$, $\epsilon_H = 2.5$. The vertical yellow lines mark the positions of the rotating drums and the blue horizontal dashed lines mark the top/bottom edges of the sample.

tion started during extension (or close to the end of extension), the light intensity would continue to increase when stopping the elongational flow, but not decrease. Therefore, the difference of onset times previously mentioned is not related to the crystallization phenomenon. Note that the intensity does not come back to the initial value, suggesting that all PP macromolecules do not relax (which is confirmed by the mean relaxation time at 133^oC, $\lambda_w = 130.6\ s$) Then, the crystallization is observed through the increase of the light intensity (birefringence induced by the semi-crystalline microstructure) strongly up to a plateau. The value of the plateau depends on the Hencky strain rate: the higher the Hencky strain rate is higher the plateau value is. This may be attributed to a larger orientation of the microstructure and an increase of crystalline fraction. The slope of the light intensity increases with the Hencky strain rate, which suggests a faster kinetics of crystallization. However, the onset time seems to be not affected. The next question relates to understanding how to quantitatively assess the kinetics of crystallization using such measurements and compare the results to those obtained for the case of a shear flow. To do so, we use the assumption that I/I_0 is proportional to the relative crystallinity. We mention at this point that we have performed no calibration measurements with a single layer of spherulites (in our case, a thickness of the sample equal to $0.3\ mm$ certainly accommodates several such layers). Yet, Koscher and Fulchiron have demonstrated that

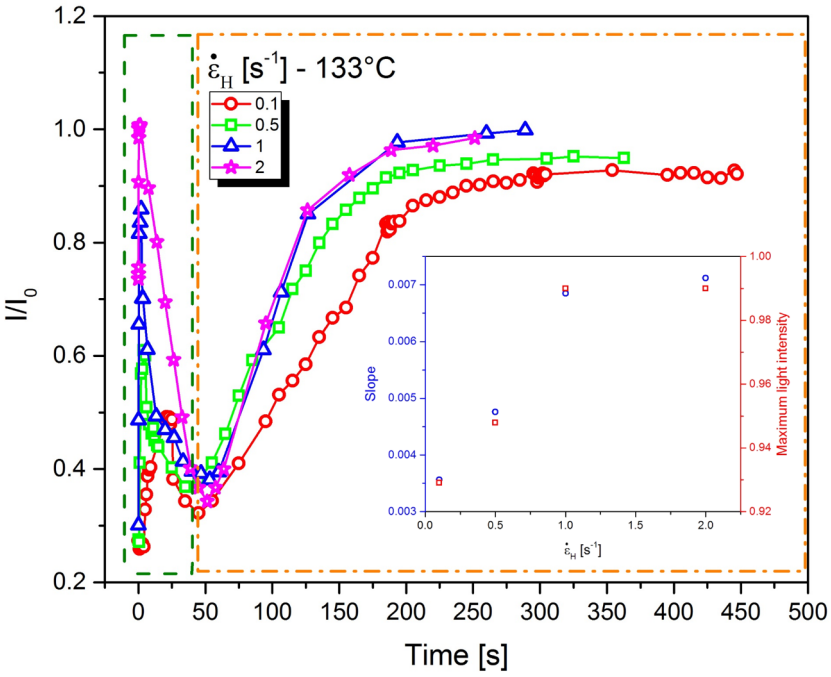

Figure 15: Light intensity evolution 133^oC, $\dot{\epsilon}_H = 0.5s^{-1}$, $\epsilon_H = 2.5$

while monitoring the isothermal crystallization using different methods (DSC, rheometry, polarized light imaging) a good agreement on the values of the half crystallization time $t_{1/2}$ is obtained, Koscher and Fulchiron (2002). Based on these considerations we chose to associate the half crystallization time to the time instant when the light intensity augments by 50%. For example, in the case of the experiment performed at an extensional rate of $0.1\ s^{-1}$, the relative light intensity when the crystallization starts is 0.31 whereas its value when full crystallization is achieved is 0.9 which, according to our method, prompts us to chose as a half crystallization time the time instant when the relative intensity is $I/I_0 = 0.605$. Nonetheless, the half-crystallization time decreases with $\dot{\epsilon}_H$ which means that the kinetics of crystallization is faster. The half time of crystallization is estimated around $100\ s$ which is significantly lower compared to the value obtained from SIC $(300\ s)$ and QC measurements $(460\ s)$ for the same rates $(0.5\ s^{-1})$ and temperature (133^oC).

From all these experiments made under different flow and temperature conditions, we are able to quantify their effect on the crystallization kinetics by comparing the crystallization half-times, as depicted in Table 2. the comparison of the half-crystallization times shows that the kinetics of crystallization under extensional deformation is divided by a factor 3 compared to the quiescent condition and after a pre-shearing, bringing a quantification of the crystallization

$\mathbf{T}(^{\mathbf{o}}\mathbf{C})$	$\dot{\gamma}$ or $\dot{\epsilon}_{\mathbf{H}}$ $(\mathbf{s^{-1}})$	Quiescent condition	Shear $G'(Pa)$	SER I/I_0
		$t_{1/2}(s)$	$t_{1/2}(s)$	$t_{1/2}(s)$
132/133	0.1	388	X	125
	0.5		311	105
	1		310	100
	2		280	100

Table 2: Half crystallization times in quiescent condition, after pre-shear and after extension

induced by extension in an *in-situ* manner.

3.3.3. SAXS and WAXS post-mortem measurements

To gain further insights into the role of extension on the crystallization process at microscopic scales, $SAXS$ and $WAXS$ measurements were performed on the polymeric samples after crystallization during extensional flow for a Hencky strain $\epsilon_H = 4$. Fig. 16 illustrates $SAXS$ and $WAXS$ measurements performed on PP samples after extension at different $\dot{\epsilon}_H$ in the middle of the sample, between the two rolls of the SER device. The extension direction is horizontal (equatorial direction) and the X-ray beam intercepted the sample between the two rolls of the SER device where the shrinkage of the cross-section is maximal ($L_0/2$). For all strain rate, $SAXS$ patterns exhibit scattering lobes around the equatorial direction in favour of an orientation of the crystalline lamellae perpendicular to the direction of flow. In addition, WAXS indicates the orientation of a crystal plane with the flow by increasing the light intensity of the diffraction rings.

The study of the orientation of each crystalline phase also shows that larger the rate of extension is stronger the orientation is. By comparing the minima and the maxima of the intensity of the scattering peaks versus the azimuthal angle, we observe that the plane (040) of the alpha phase is more oriented than the planes (110) and (300) - see Figs. 22, 23 in Sec. 6. The stronger orientation of the plane (040) may be explained by the assumption of populations of mother crystalline lamellae and daughter ones which is typically observed with iPP. The planes (040) of mother and daughter lamellae are oriented in the same direction whereas the planes (110) of both kinds of lamellae have a double orientation. The $WAXS$ measurements were performed along a single direction of the sample and do not provide information on the orientation of the planes (110) et (300). Thus, to quantify the orientation of the other crystalline planes one needs to perform scattering experiments along several other directions of the sample.

From $SAXS$ patterns, the characteristic size of the lamellar structure is given by the long period L_p and is defined as $L_p = \frac{2\pi}{q_{max}}$, where q_{max} is the value of the wave vector for the scattering peak (see Fig. 17). This value is

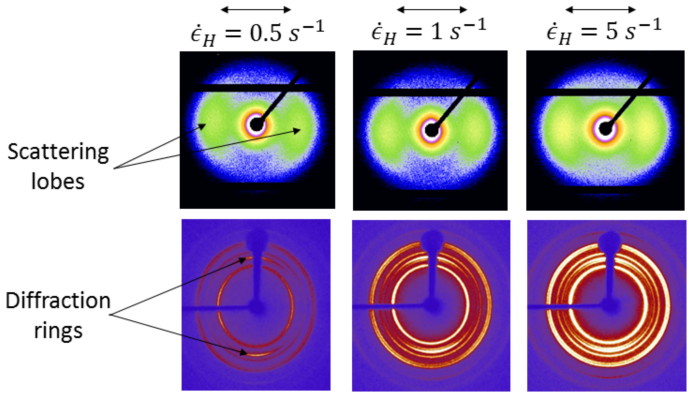

Figure 16: $2D\ SAXS$ and $2D\ WAXS$ patterns of samples that undergone an esxtensional flow at $T = 133\ ^oC$ and several rates of deformation: a) $\dot{\epsilon}_H = 0.5\ s^{-1}$, b) $\dot{\epsilon}_H = 1\ s^{-1}$, c) $\dot{\epsilon}_H = 5\ s^{-1}$. In each panel the arrow indicates the flow direction.

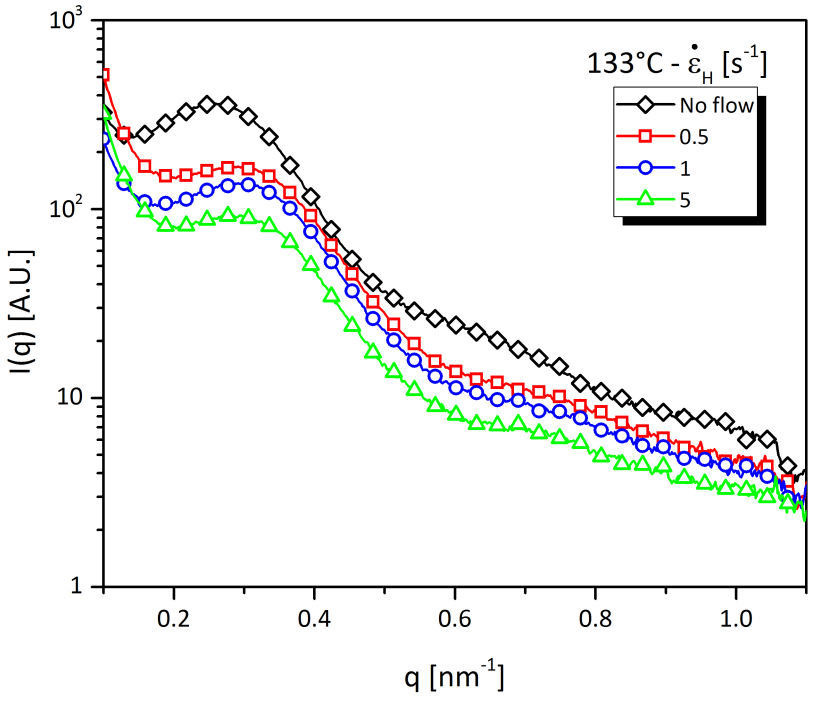

Figure 17: 1D $SAXS$ data after azimutal averaging of scattering lobes observed in Fig. 16. The terminal Hencky strain was ϵ_H=4

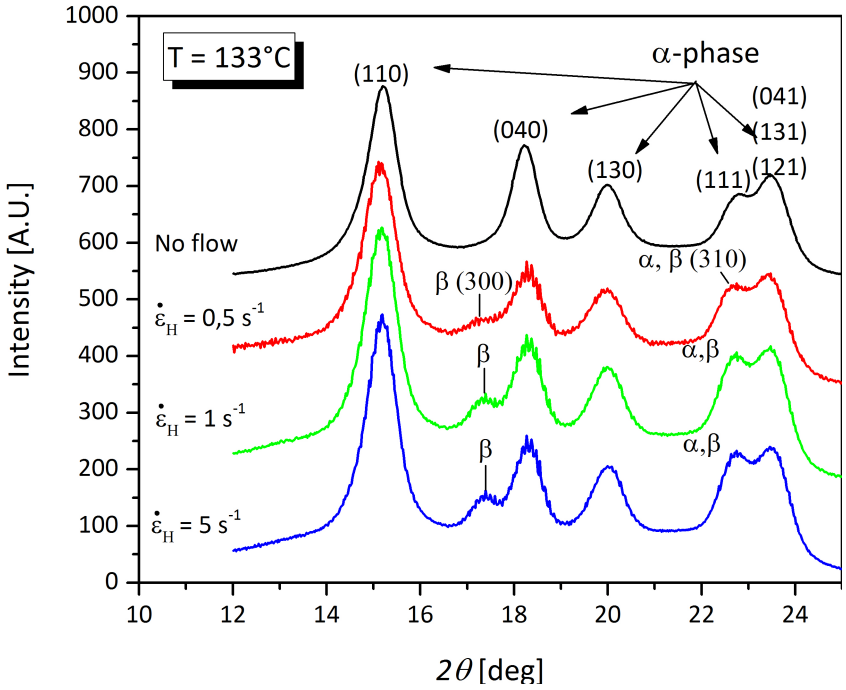

Figure 18: $WAXS$ patterns measured for different Hencky extension rates at $133\ ^oC$

accurately determined by plotting $q^2 \times I(q)$ vs. q. The long period of the unstretched sample is approximately $21\ nm$. In the case of a stretched sample, with increasing extension rates from 0.5 to $5\ s^{-1}$, L_p was found to decrease from $18.3\ nm$ to $18.00\ nm$, which is not significant. Note that for all samples the thermal history remains the strictly the same. Quite obviously, L_p is not sensitive to the rate of extension but mostly to the presence or absence of flow. The thickness if lamellae is therefore controlled by the temperature.

The $WAXS$ analysis also shows the formation of the β-phase (in addition of the α-phase) with a higher content when the rate of extension increases as shown in Fig. 18.

A next interesting issue to be addressed is how the microstructure and lamellar orientation revealed by the $SAXS$ and $WAXS$ measurements relates to the horizontal position along the sample. During an experiment, all the polymer flows at the imposed strain rate but the elongational deformation is stopped when it starts to be in contact with the drum. So, after the experiment, the Hencky strain will be maximum ($\epsilon_H = 4$) at the center of the extended sample, whereas it will be smaller when we move away from this position. At large Hencky strains the sample is slightly narrower close to the centre than close to the edges which implies that the rate of deformation is higher close to the centre and smaller close to the edges as shown in Amirdine et al. (2019). To address this

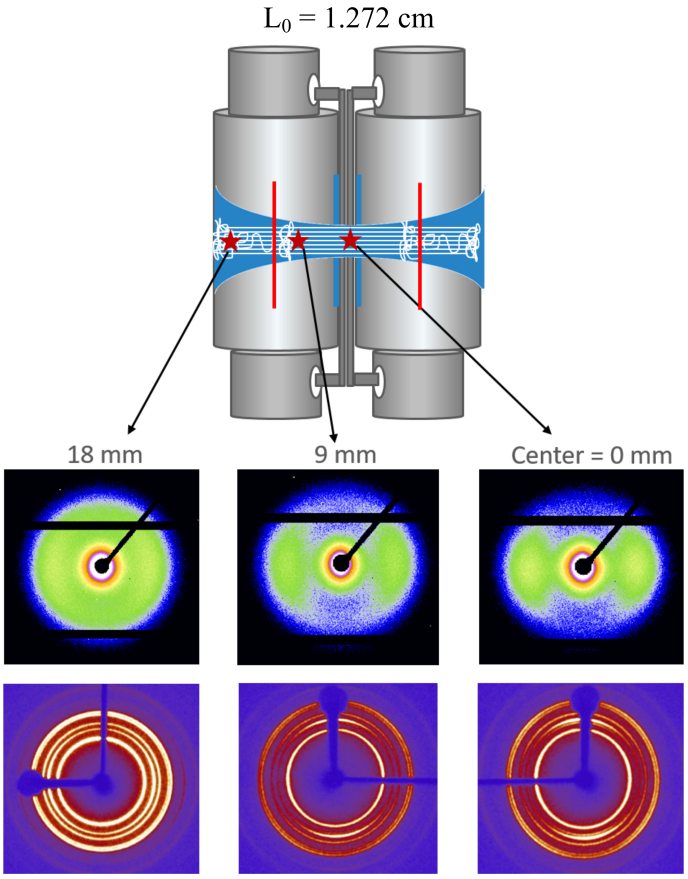

Figure 19: $2D$ $SAXS$ and $2D$ $WAXS$ patterns measured at 133 ^oC, $\dot{\epsilon}_H = 1\ s^{-1}$, $\epsilon_H = 4$ and several positions from the centres marked by the stars in the top panel and indicated in the inserts of the lower panels.

question, *post-mortem* $SAXS$ and $WAXS$ measurements were carried out at different positions along the sample as schematically illustrated in the top panel of Fig. 19.

Indeed, the $SAXS$ patterns presented in Fig. 19 clearly indicate that close to the centre of the sample, where the local rate of extension and the Hencky strain are the largest, the orientation is the strongest. This analysis then shows that the deformation is geometrically homogeneous and maximum at this position. Indeed, when approaching the fastening clips, the sample undergoes both shear and extension whereas in the centre of the sample, the sample undergoes pure uniaxial extensional deformation. According to the $WAXS$ measurements, the beta phase appears beyond a critical Hencky strain rate and where the elongation is maximum (at the centre of the sample).

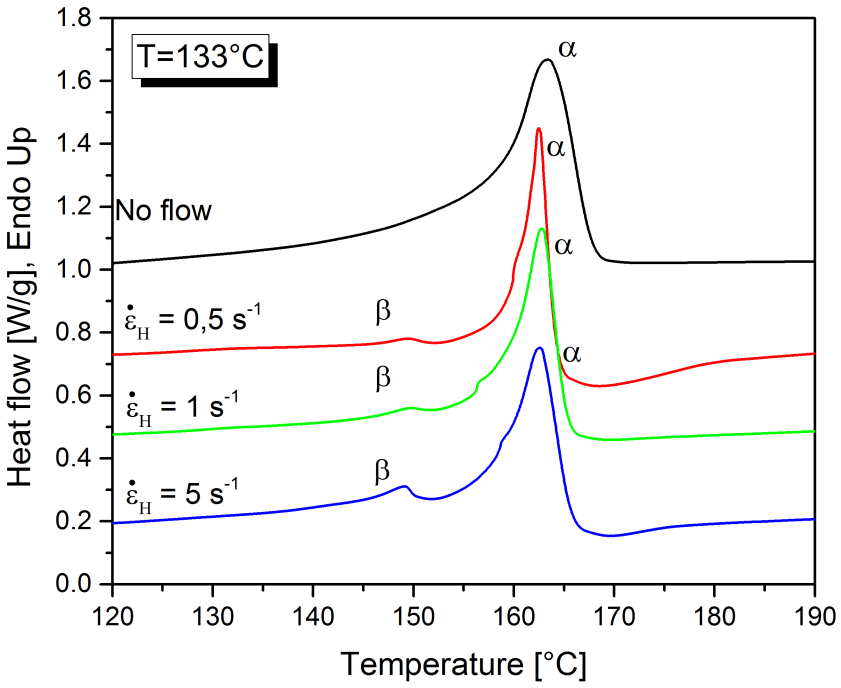

Figure 20: DSC measurements performed with a sample extended up to Hencky strain $\epsilon_H = 4$ at $9\ mm$ from its centre.

3.3.4. Post mortem DSC measurements

Fig. 20 shows DSC measurements performed on the samples for a deformation of 4 at $133\ ^oC$. The black line represents a sample before the extensional flow. Besides, DSC curves present clearly first a main melting peak and also a second one whose intensity increases with the rate. The major melting peak is around a temperature of $162\ ^oC$ and the minor is around 148^oC. iPP is a polymorphic polymer and flow can influence the crystal structure. In quiescent condition, only α-phase can be observed and for high cooling rates mesophase can also be obtained by FSC Schawe et al. (2017). However, under shear flow or extensional flow, β-phase can appear as explained by Liu et al. (2013). So the major peak is attributed to the α-phase and the minor to the β-phase according to Koscher (2002), which is also coherent with $WAXS$ data.

As previously shown with $SAXS$ and $WAXS$ measurements, the microstructure and orientation depend on the horizontal position along the sample. Close to the centre (i.e. between the two rolls of SER apparatus), the orientation is larger since the Hencky strain is larger at this position compared to the other ones, with a homogeneous elongational flow. The β-phase seems to be more present close to the middle, where extensional deformation is larger and more pure (i.e. no shear is superposed).

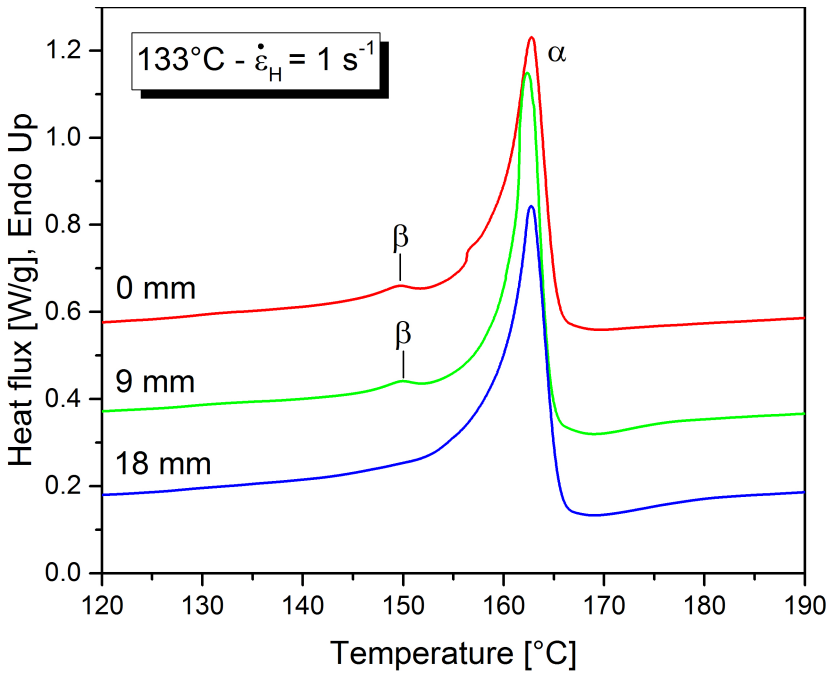

Figure 21: DSC measurements, $\epsilon_H = 4$, $\dot{\epsilon}_H = 1\ s^{-1}$ for different positions

4. Conclusions, outlook

A characterization of the crystallization induced by extensional flow is presented. The crystallization of PP under quiescent condition and after pre-shear are first presented. This experimental characterization allows one to obtain the half-crystallization times and relate them to the deformation conditions. To study the crystallization induced by extension, a modified SER apparatus is used. The modification consists in equipping the device with an oil bath with transparent walls. This modification allows the *in-situ* visualization of the sample and limits the gravity sagging and ensures a better homogeneity of the temperature distribution within the sample. The kinetics of crystallization was monitored *in-situ* via polarized light imaging of the sample. The estimation of a half-crystallization time indicates an acceleration of the kinetics of crystallization by a factor of 3 as compared to the crystallisation under shear. Post-mortem characterization of the samples is performed by both X-ray scattering and DSC measurements. An agreement with previously published results is found. The microstructure is oriented in the direction of flow and the crystalline lamellae are oriented perpendicular to the direction of flow. However, the $SAXS$ measurements indicate no evidence of shish-kebab microstructres. The *post-mortem* analysis also reveals the formation of the β crystalline phase in addition to the majority α phase. The analysis of the *post-mortem* sample at different axial positions reveals a spatial

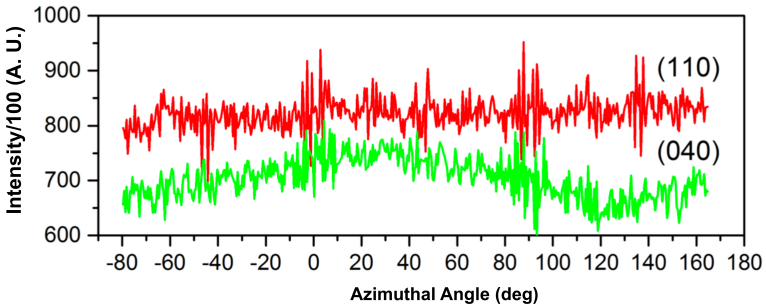

Figure 22: Dependence of the $WAXS$ intensity on azimuthal angle for the planes (110), (040) (alpha phase) measured after crystallization at 133^oC without elongation.

gradient of the microstructure which is consistent with a gradient of Hencky strain (since the elongation is stopped when the sample is in contact with a roll of the SER apparatus) and an extensional process, which can be slightly kinematically non-uniform.

5. Acknowledgements

We gratefully acknowledge the Agence Nationale de la Recherche (ANR) for the financial support via project KinHeTeX ($ANR-16-CE08-0022-01$). We thank M. Ruben Vera (Centre de Diffractométrie Henri Longchambon, Université Claude Bernard Lyon 1) for $WAXS$ Analyses.

6. Annex

Figures 22 and 23 show the $WAXS$ intensity as a function of the azimuthal angle for both non-stretched and stretched at $5\ s^{-1}$ samples, respectively. Again, the lamellae orientation is revealed by these intensity variations. However, the variation for the 040 peak is much more important than this of the 100 peak. This is generally the case for i-PP when mother-daughter lamellae are present, as shown by Fiorentino and coworkers, Fiorentino et al. (2013).

Figure 24 shows the $WAXS$ intensity of the 040 peak as a function of the azimuthal angle for the 3 different positions corresponding to different total strains. It appears from the variation amplitudes between 0^o and 90^o azimuthal angles that the orientation is higher for the position "0" which corresponds to the maximum deformation ($\epsilon_H = 4$).

References

Adamovsky, S.A., Minakov, A.A., Schick, C., 2003. Scanning microcalorimetry at high cooling rate. Thermochim. Acta 403, 55–63. doi:10.1016/S0040-6031(03)00182-5.

Amirdine, J., Burghelea, T., Boyard, N., Amirdine, J., Burghelea, T., Bo-

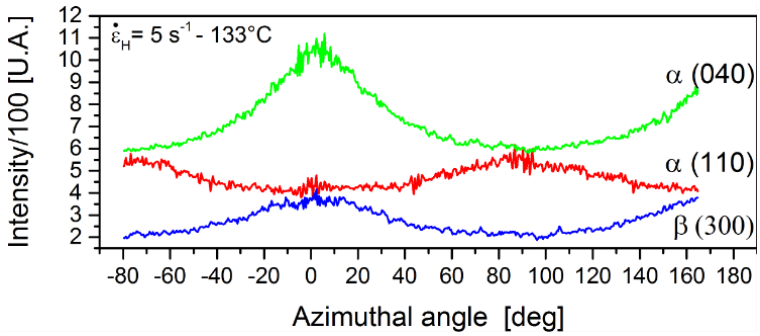

Figure 23: $WAXS$ intensity versus azimuthal angle for (110), (040) (alpha phase) and (300) (beta phase) planes after crystallization at 133^oC for an Hencky strain rate at $5s^{-1}$. The curves are shifted for better clarity.

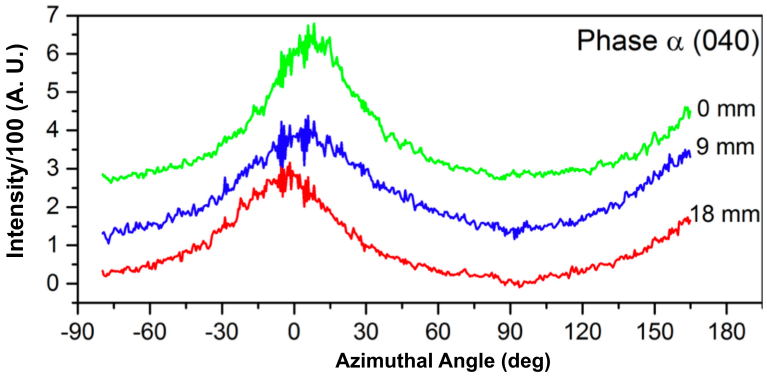

Figure 24: $WAXS$ intensity versus azimuthal angle for (110), (040) (alpha phase) after crystallization at 133^oC for an Hencky strain rate at $5s^{-1}$ for 3 different positions along the specimen : $0mm$(center), $9mm$ and $18mm$. The curves are shifted for better clarity.

yard, N., 2019. Effet d'une déformation extensionnelle sur la cinétique de cristallisation de polymères semi-cristallins To cite this version : HAL Id : hal-02420808, in: 21ème Journées Natl. sur les Compos. École Natl. Supérieure d'Arts Métiers - Bordeaux, Jul 2019, Bordeaux, Talence, Fr. URL: https://hal.archives-ouvertes.fr/hal-02420808.

Angelloz, C., Fulchiron, R., Douillard, A., Chabert, B., Fillit, R., Vautrin, A., David, L., 2000. Crystallization of isotactic polypropylene under high pressure (Gamma phase). Macromolecules 33, 4138–4145. doi:10.1021/ma991813e.

Avrami, M., 1939. Kinetics of Phase Change. I - General Theory. J. Chem. Phys. 7, 1103–1112.

Avrami, M., 1940. Kinetic of Phase Change II - Transformation-Time Relations for Random Distribution of Nuclei. J. Chem. Phys. 8, 212–224.

Avrami, M., 1941. Granulation, Phase Change, and Microstructure - Kinetics of Phase Change III. J. Chem. Phys. 9, 177–184.

Bach, A., Rasmussen, H.K., Longin, P.Y., Hassager, O., 2002. Growth of non - axisymmetric disturbances of the free surface in the filament stretching rheometer: Experiments and simulation. J. Nonnewton. Fluid Mech. 108, 163–186. doi:10.1016/S0377-0257(02)00129-5.

Boyer, S.A.E., Grolier, J.P.E., Yoshida, H., Haudin, J.M., Chenot, J.L., 2011. Thermodynamics and Thermokinetics to Model Phase Transitions of Polymers over Extended Temperature and Pressure Ranges under Various Hydrostatic Fluids, in: Moreno-Pirajan, J.C. (Ed.), Thermodyn. Stud. Gases. URL: https://www.intechopen.com/books/thermodynamics-interaction-studies-solids-liquids-and-gases/thermodynamics-and-thermokinetics-to-model-phase-transitions-of-polymers-over- doi:10.5772/823.

Burghelea, T.I., Grieß, H.J., Münstedt, H., 2012. An in situ investigation of the draw resonance phenomenon in film casting of a polypropylene melt. J. Nonnewton. Fluid Mech. 173-174, 87–96. URL: http://dx.doi.org/10.1016/j.jnnfm.2012.02.006, doi:10.1016/j.jnnfm.2012.02.006.

Chellamuthu, M., Arora, D., Winter, H.H., Rothstein, J.P., 2011. Extensional flow-induced crystallization of isotactic poly-1-butene using a filament stretching rheometer. J. Rheol. (N. Y. N. Y). 55, 901–920. URL: http://sor.scitation.org/doi/10.1122/1.3593471, doi:10.1122/1.3593471.

De Santis, F., Adamovsky, S., Titomanlio, G., Schick, C., 2006. Scanning nanocalorimetry at high cooling rate of isotactic polypropylene. Macromolecules 39, 2562–2567. doi:10.1021/ma052525n.

Derakhshandeh, M., Hatzikiriakos, S.G., 2012. Flow-induced crystallization of high-density polyethylene: The effects of shear and uniaxial extension. Rheol. Acta 51, 315–327. doi:10.1007/s00397-011-0605-7.

Eder, G., Janeschitz-Kriegl, H., Liedauer, S., 1990. Crystallization processes in quiescent and moving polymer melts under heat transfer conditions. Progress in Polymer Science 15, 629 – 714. URL: http://www.sciencedirect.com/science/article/pii/0079670090900080, doi:https://doi.org/10.1016/0079-6700(90)90008-O.

Fiorentino, B., Fulchiron, R., Duchet-Rumeau, J., Bounor-Legaré, V., Majesté, J.C., 2013. Controlled shear-induced molecular orientation and crystallization in polypropylene/talc microcomposites – effects of the talc nature. Polymer 54, 2764 – 2775. URL: http://www.sciencedirect.com/science/article/pii/S0032386113002760, doi:https://doi.org/10.1016/j.polymer.2013.03.057.

Hadinata, C., Boos, D., Gabriel, C., Wassner, E., Rullmann, M., Kao, N., Laun, M., 2007. Elongation-induced crystallization of a high molecular weight isotactic polybutene-1 melt compared to shear-induced crystallization. J. Rheol. (N. Y. N. Y). 51, 195. doi:10.1122/1.2426977.

Hadinata, C., Gabriel, C., Ruellman, M., Laun, H.M., 2005. Comparison of shear-induced crystallization behavior of PB-1 samples with different molecular weight distribution. J. Rheol. (N. Y. N. Y). 49, 327–349. doi:10.1122/1.1835342.

Ianniruberto, G., Marrucci, G., Masubuchi, Y., 2020. Melts of linear polymers in fast flows. Macromolecules 53, 5023–5033. URL: https://doi.org/10.1021/acs.macromol.0c00693, doi:10.1021/acs.macromol.0c00693, arXiv:https://doi.org/10.1021/acs.macromol.0c00693.

Janeschitz-Kriegl, H., Ratajski, E., 2005. Kinetics of polymer crystallization under processing conditions: Transformation of dormant nuclei by the action of flow. Polymer 46, 3856–3870. doi:10.1016/j.polymer.2005.02.096.

Karpp-Pfordt, S., 2006. Cristallisation induite par cisaillement du MXD6 dans différentes formulations (additifs nucléants, fibres de verre). Ph.D. thesis. Université Claude Bernard - Lyon 1.

Koscher, E., 2002. Effets du cisaillement sur la cristallisation du polypropylène : aspects cinétiques et morphologiques. Ph.D. thesis. Université Claude Bernard Lyon 1.

Koscher, E., Fulchiron, R., 2002. Influence of shear on polypropylene crystallization: morphology development and kinetics. Polymer 43, 6931–6942. doi:10.1140/epje/12004-10046-8.

Lagasse, R.R., Maxwell, B., 1976. An experimental study of the kinetics of polymer crystallization during shear flow. Polymer Engineering & Science 16, 189–199. URL: https://onlinelibrary.wiley.com/doi/abs/10.1002/pen.760160312, doi:https://doi.org/10.1002/pen.760160312, arXiv:https://onlinelibrary.wiley.com/doi/pdf/10.1002/pen.760160312.

Lamberti, G., De Santis, F., Brucato, V., Titomanlio, G., 2004. Modeling the interactions between light and crystallizing polymer during fast cooling. Applied Physics A 78, 895–901. URL: https://doi.org/10.1007/s00339-003-2086-8, doi:10.1007/s00339-003-2086-8.

Liu, D., Tian, N., Huang, N., Cui, K., Wang, Z., Hu, T., Yang, H., Li, X., Li, L., 2014. Extension-induced nucleation under near-equilibrium conditions: The mechanism on the transition from point nucleus to shish. Macromolecules 47, 6813–6823. doi:10.1021/ma501482w.

Liu, Q., Sun, X., Li, H., Yan, S., 2013. Orientation-induced crystallization of isotactic polypropylene. Polymer 54, 4404–4421. URL: http://dx.doi.org/10.1016/j.polymer.2013.04.066, doi:10.1016/j.polymer.2013.04.066.

Liu, Y., Zhou, W., Cui, K., Tian, N., Wang, X., Liu, L., Li, L., Zhou, Y., 2011. Extensional rheometer for in situ x-ray scattering study on flow-induced crystallization of polymer. Review of Scientific Instruments 82, 045104. URL: https://doi.org/10.1063/1.3574219, doi:10.1063/1.3574219, arXiv:https://doi.org/10.1063/1.3574219.

McHugh, A.J., 1995. Flow induced crystallization in polymers In Rheo-physics of multiphase polymeric systems. Lancaster ed., Technomic Publishing Co.

Meissner, J., Hostettler, J., 1994. A new elongational rheometer for polymer melts and other highly viscoelastic liquids. Rheol. Acta 33, 1–21. doi:10.1007/BF00453459.

Mileva, D., Androsch, R., Zhuravlev, E., Schick, C., Wunderlich, B., 2012. Homogeneous nucleation and mesophase formation in glassy isotactic polypropylene. Polymer 53, 277–282. URL: http://dx.doi.org/10.1016/j.polymer.2011.11.064, doi:10.1016/j.polymer.2011.11.064.

Muke, S., Ivanov, I., Kao, N., Bhattacharya, S.N., 2001. Extensional rheology of polypropylene melts from the Rheotens test. J. Nonnewton. Fluid Mech. 101, 77–93. doi:10.1016/S0377-0257(01)00142-2.

Münstedt, H., Laun, H.M., 1979. Elongational behaviour of a low density polyethylene melt - II. Transient behaviour in constant stretching rate and tensile creep experiments. Comparison with shear data. Temperature dependence of the elongational properties. Rheol. Acta 18, 492–504. doi:10.1007/BF01736955.

Naudy, S., David, L., Rochas, C., Fulchiron, R., 2007. Shear induced crystallization of poly(m-xylylene adipamide) with and without nucleating additives. Polymer 48, 3273–3285. doi:10.1016/j.polymer.2007.03.076.

Oukaci-Boukellal, G., 2010. Détermination des paramètres non linéaires constitutifs de lois de comportement viscoélastique par mesures de champ dans des écoulements complexes. Ph.D. thesis. Ecole des Mines de Paris.

Roozemond, P.C., Van Erp, T.B., Peters, G.W., 2016. Flow-induced crystallization of isotactic polypropylene: Modeling formation of multiple crystal phases and morphologies. Polymer 89, 69–80. URL: http://dx.doi.org/10.1016/j.polymer.2016.01.032, doi:10.1016/j.polymer.2016.01.032.

S. A. E. Boyer, S., Haudin, J.M., 2010. Crystallization of polymers at constant and high cooling rates: A new hot-stage microscopy set-up. Polym. Test. 29, 445–452. URL: http://dx.doi.org/10.1016/j.polymertesting.2010.02.003, doi:10.1016/j.polymertesting.2010.02.003.

S. A. E. Boyer, S., Robinson, P., Ganet, P., Melis, J.P., Haudin, J.M., 2012. Crystallization of Polypropylene at High Cooling Rates: Microscopic and Calorimetric Studies. Polym. Polym. Compos. 125, 4219–4232. doi:10.1002/app, arXiv:1206.4529.

Schawe, J.E., 2015. Analysis of non-isothermal crystallization during cooling and reorganization during heating of isotactic polypropylene by fast scanning DSC. Thermochim. Acta 603, 85–93. doi:10.1016/j.tca.2014.11.006.

Schawe, J.E., Pötschke, P., Alig, I., 2017. Nucleation efficiency of fillers in polymer crystallization studied by fast scanning calorimetry: Carbon nanotubes

in polypropylene. Polymer 116, 160–172. doi:10.1016/j.polymer.2017.03.072.

Schneider, W., Köppl, A., Berger, J., 1988. Non-Isothermal Crystallization – Crystallization of Polymers – System of Rate Equations.

Sentmanat, M., Delgadillo-Velázquez, O., Hatzikiriakos, S.G., 2010. Crystallization of an ethylene-based butene plastomer: The effect of uniaxial extension. Rheol. Acta 49, 931–939. doi:10.1007/s00397-010-0461-x.

Sentmanat, M.L., 2004. Miniature universal testing platform: From extensional melt rheology to solid-state deformation behavior. Rheol. Acta 43, 657–669. doi:10.1007/s00397-004-0405-4.

Stadler, F.J., Kaschta, J., Münstedt, H., Becker, F., Buback, M., 2009. Influence of molar mass distribution and long-chain branching on strain hardening of low density polyethylene. Rheol. Acta 48, 479–490. doi:10.1007/s00397-008-0334-8.

Stary, Z., Papp, M., Burghelea, T., 2015. Deformation regimes, failure and rupture of a low density polyethylene (LDPE) melt undergoing uniaxial extension. J. Nonnewton. Fluid Mech. 219, 35–49. doi:10.1016/j.jnnfm.2015.02.007.

Szabo, P., McKinley, G., 2003. Filament stretching rheometer: inertia compensation revisited. Rheol. Acta 42, 269–272. URL: http://dx.doi.org/10.1007/s00397-002-0277-4, doi:10.1007/s00397-002-0277-4.

Tardif, X., Pignon, B., Boyard, N., Schmelzer, J.W.P., Sobotka, V., Delaunay, D., Schick, C., 2014. Experimental study of crystallization of PolyEtherEtherKetone (PEEK) over a large temperature range using a nano-calorimeter. Polym. Test. 36, 10–19. URL: http://dx.doi.org/10.1016/j.polymertesting.2014.03.013, doi:10.1016/j.polymertesting.2014.03.013.

Tian, N., Zhao, B., Li, X., Liu, Y., Zhou, W., Cui, K., Liu, D., Li, L., 2013. Confined crystallization in end-linked PEO network under uniaxial extension. Polymer 54, 7088–7093. URL: http://dx.doi.org/10.1016/j.polymer.2013.10.055, doi:10.1016/j.polymer.2013.10.055.

Tian, N., Zhou, W., Cui, K., Liu, Y., Fang, Y., Wang, X., Liu, L., Li, L., 2011. Extension flow induced crystallization of poly(ethylene oxide). Macromolecules 44, 7704–7712. doi:10.1021/ma201263z.

Wang, Z., Ma, Z., Li, L., 2016. Flow-Induced Crystallization of Polymers: Molecular and Thermodynamic Considerations. Macromolecules 49, 1505–1517. doi:10.1021/acs.macromol.5b02688.

White, E.E.B., Winter, H., Rothstein, J.P., 2012. Extensional-flow-induced crystallization of isotactic polypropylene. Rheol. Acta 51, 303–314. doi:10.1007/s00397-011-0595-5.

Zhuravlev, E., Schick, C., 2010a. Fast scanning power compensated differential scanning nano-calorimeter: 1. The device. Thermochim. Acta 505, 1–13. URL: http://dx.doi.org/10.1016/j.tca.2010.03.019, doi:10.1016/j.tca.2010.03.019.

Zhuravlev, E., Schick, C., 2010b. Fast scanning power compensated differential scanning nano-calorimeter: 2. Heat capacity analysis. Thermochim. Acta 505, 1–13. URL: http://dx.doi.org/10.1016/j.tca.2010.03.020, doi:10.1016/j.tca.2010.03.019.